Click Here for Full Article

Global marine gravity from retracked Geosat and ERS-1 altimetry: Ridge segmentation versus spreading rate

David T. Sandwell[1] and Walter H. F. Smith[2]

[1]   Three approaches are used to reduce the error in the satellite-derived marine gravity anomalies. First, we have retracked the raw waveforms from the ERS-1 and Geosat/GM missions resulting in improvements in range precision of 40% and 27%, respectively. Second, we have used the recently published EGM2008 global gravity model as a reference field to provide a seamless gravity transition from land to ocean. Third, we have used a biharmonic spline interpolation method to construct residual vertical deflection grids. Comparisons between shipboard gravity and the global gravity grid show errors ranging from 2.0 mGal in the Gulf of Mexico to 4.0 mGal in areas with rugged seafloor topography. The largest errors of up to 20 mGal occur on the crests of narrow large seamounts. The global spreading ridges are well resolved and show variations in ridge axis morphology and segmentation with spreading rate. For rates less than about 60 mm/a the typical ridge segment is 50–80 km long while it increases dramatically at higher rates (100–1000 km). This transition spreading rate of 60 mm/a also marks the transition from axial valley to axial high. We speculate that a single mechanism controls both transitions; candidates include both lithospheric and asthenospheric processes.

1.   Introduction

[2]   Marine gravity anomalies derived from radar altimeter measurements of ocean surface slope are the primary data for investigating global tectonics and continental margin structure [*Cande et al.*, 2000; *Fairhead et al.*, 2001; *Lawler et al.*, 1992; *Laxon and McAdoo*, 1994; *Mueller et al.*, 1997]. In addition, altimeter-derived gravity has been combined with sparse ship soundings to construct global bathymetry grids [*Baudry and Calmant*, 1991; *Dixon et al.*, 1983; *Jung and Vogt*, 1992; *Ramillien and Cazenave*, 1997; *Smith and Sandwell*, 1994, 1997]. The bathymetry and seafloor roughness vary throughout the oceans as a result of numerous geologic processes [*Brown et al.*, 1998]. This seafloor topography influences the ocean circulation and mixing that moderate Earth's climate [*Jayne et al.*, 2004; *Kunze and Llewellyn Smith*, 2004; *Munk and Wunch*, 1998] and the biological diversity and food resources of the sea.

[3]   While these satellite altimeter data are enormously valuable for exploring the remote ocean basins, the amount of geodetically useful data that has been collected is comparatively small. To date, eight high-precision radar altimeter missions (Geosat 1985–1989, ERS-1 1991–1998, Topex/Poseidon 1992–2006, ERS-2 1995–present, GFO,

1998–present, Jason 1, 2001–present, ENVISAT 2002–present, and Jason 2 2008–present) have logged 63 years of sea surface height measurements. However, only a small fraction (2.4 years or 4%) of these data have spatially dense ground tracks that are suitable for gravity field recovery. Most of the 63 years of altimeter data were collected from the repeat orbit configuration that is optimal for recovering changes in ocean surface height associated with currents and tides [*Fu and Cazenave*, 2001]. The only sources of nonrepeat altimeter data are the geodetic phases of Geosat (18 months) and ERS-1 (11 months). These nonrepeat profiles, combined with "stacks" (temporal averages) of repeat profiles from the other altimeters, have been used in numerous studies to estimate the short wavelengths (<400 km) of the marine gravity field [*Andersen and Knudsen*, 1998; *Cazenave et al.*, 1996; *Hwang and Parsons*, 1996; *Sandwell and Smith*, 1997; *Tapley and Kim*, 2001]. The longer wavelength gravity field is more accurately measured at orbital altitude using spacecraft such as CHAMP [*Reigber et al.*, 2002], GRACE [*Tapley et al.*, 2005], and GOCE [*Klees et al.*, 2000].

[4]   Because of this limited supply of data, the geodetic community has made every effort to improve the accuracy and resolution of the nonrepeat phases of the Geosat and ERS-1 missions. For recovery of the static marine gravity field, the critical measurement is the slope of the ocean surface. Laplace's equation combined with Bruns' formula shows that one microradian (μrad) of ocean surface slope roughly corresponds to 1 milligal (mGal) of gravity anomaly [*Haxby et al.*, 1983]. Ocean surface slope can be estimated by differencing height measurements along satel-

[1]Scripps Institution of Oceanography, University of California, San Diego, La Jolla, California, USA.
[2]Laboratory for Satellite Altimetry, NOAA, Silver Spring, Maryland, USA.

lite altimeter profiles so absolute range accuracy is largely irrelevant [*Sandwell*, 1984]. Indeed the usual corrections and ancillary data that are needed to recover the temporal variations in ocean surface height associated with currents and eddies are largely unimportant for the recovery of the gravity field because the slope of these corrections is far less than the slope error in the radar altitude measurement.

[5] One way of improving the range precision of the altimeter data is to retrack the raw altimeter waveform. Standard waveform retracking estimates three to five parameters, the most important being arrival time, risetime or significant wave height (SWH), and return amplitude [*Amarouche et al.*, 2004; *Brown*, 1977]. Arrival time and SWH are inherently correlated because of the noise characteristics of the return waveform [*Maus et al.*, 1998; *Sandwell and Smith*, 2005]. Two previous studies have demonstrated up to 40% improvement in range precision by optimizing the retracking algorithm to achieve high range precision at the expense of recovering small spatial scale variations in ocean wave height [*Maus et al.*, 1998; *Sandwell and Smith*, 2005]. We have retracked the ERS-1 altimeter waveform data for all of the geodetic phase and part of the 35-day-repeat phase, and we have made these retracked data available to the scientific community. These retracked ERS-1 data were used to construct a new marine gravity model for investigating the relationship between linear volcanic chains and 150 km wavelength gravity lineations in the Central South Pacific [*Sandwell and Fialko*, 2004] discovered by *Haxby and Weissel* [1986].

[6] In this study we make three additional improvements to the accuracy and resolution of the global marine gravity field. First, we retrack all the altimeter waveforms from the Geosat Geodetic Mission (GM) using a two-step algorithm similar to the algorithm we developed for retracking the ERS-1 data [*Sandwell and Smith*, 2005]. Recently, *Lillibridge et al.* [2004] have completed a major upgrade of the GM data by constructing a new Geosat data product. This product comprises the original sensor data records with the waveform data records, yielding a complete data set at the full (10 Hz) sampling rate. This data set includes the original radar range measurements made by the onboard "alpha-beta" tracker, and the returned radar power ("waveforms"), so that the latter may be reprocessed ("retracked") and compared with the former.

[7] The second improvement to the global marine gravity field is to grid the along-track slope data into a consistent surface using a biharmonic spline interpolation algorithm. Our previous satellite gravity grids [*Sandwell and Smith*, 1997] used an iterative approach [*Menke*, 1991] to calculate a surface that is consistent with all this slope data. Here we use a 2-D biharmonic Greens functions approach originally developed by *Sandwell* [1987] to combine slopes from noisy GEOS-3 radar altimeter profiles with more precise slopes from Seasat profiles. This method has been extended by *Wessel and Bercovici* [1998] to also include a tension parameter which helps to suppress spline overshoots in areas of sharp gradient.

[8] Our third improvement is the use of a new global geopotential model, EGM2008, complete to spherical harmonic degree 2160, for the remove/restore procedure [*Pavlis et al.*, 2007]. Previously, we used EGM96 [*Lemoine et al.*, 1998] to degree and order 360. The higher spatial resolution of EGM2008 results in a major improvement in gravity near shorelines. An estimate of the mean ocean dynamic topography (MDOT) included with EGM2008 corrects a portion of the sea surface slope associated with western boundary currents resulting in a 6–10 mGal improvement in gravity anomaly accuracy in these areas.

2. Data Analysis
2.1. Retracking Altimeter Waveforms

[9] As mentioned above and discussed more fully in several previous publications [e.g., *Sandwell*, 1984; *Rummel and Haagmans*, 1990; *Hwang and Parsons*, 1996; *Sandwell and Smith*, 1997; *Andersen and Knudsen*, 1998], the accuracy of the gravity field derived from satellite altimetry is proportional to the accuracy of the local measurement of ocean surface slope. Since the height of the ocean surface at a particular location varies with time because of tides, currents, and atmospheric pressure, the most accurate slope measurements are from continuous altimeter profiles. Consider the recovery of a 1 mGal accuracy gravity anomaly having a wavelength of 28 km. This requires a sea surface slope accuracy of 1 microradian (μrad) over a 7 km length scale (1 s of flight along the satellite track), necessitating a height precision of 7 mm in one-per-second measurements of sea surface height. Current satellite altimeters with standard onboard waveform tracking such as Geosat, ERS-1/2, and Topex have typical 1-s averaged range precision of 30–40 mm resulting in gravity field accuracies of 4–6 mGal.

[10] A more serious issue with the onboard waveform trackers is that they must perform the tracking operation in real time using a so-called alpha-beta tracking loop. The Geosat onboard tracker acts as a critically damped oscillator with a resonance around 0.4 Hz and a group delay of about 0.25 s. Sea surface heights computed from the onboard tracker's range estimates thus have amplified noise in a band centered around 18 km wavelength, while local extrema in height are displaced about 1.7 km down-track of their true position. Retracking eliminates the resonance and the delay, placing features at the proper location along the ground track and sharpening the focus on small-scale features.

[11] The retracking method employed here is two step: first, a five-parameter waveform model (Figure 1) is fit to each 10-Hz waveform, solving for arrival time (t_o), risetime (σ), amplitude (A), prearrival noise floor (N), and trailing-edge plateau decay (κ). In the second pass of retracking, along-track smoothed values of all the parameters except the range arrival time, t_0, are formed and a one-parameter fit of the arrival time is made with the other four parameters set to their smoothed values. This has the desirable effect of decoupling noise in the estimation of range from noise in the estimation of the risetime.

[12] To illustrate the inherent correlation between errors in estimated arrival time and errors in estimated risetime, we performed a Monte Carlo experiment simulating model fitting to noisy data [*Sandwell and Smith*, 2005]. In the experiment we generated 2000 realizations of noisy waveforms, each waveform having the same known true parameters for arrival time, risetime, and amplitude, plus a realistic power-dependent random noise. We then did a
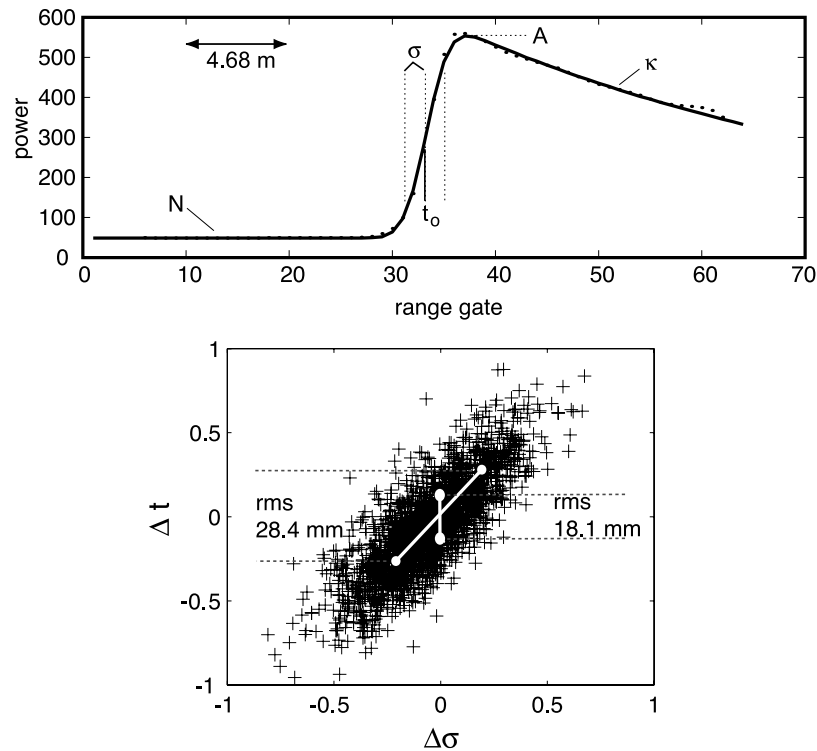
Figure 1. (top) Average of 10,000 Geosat radar waveforms (dotted) and a simplified model with five adjustable parameters: A, amplitude; t_o, arrival time; σ, risetime; N, leading edge noise floor; κ, trailing edge decay. The spacing of the gates is 3.12 ns or 468. mm. (bottom) Error in estimated arrival time versus error in estimated risetime for a synthetic experiment using realistic waveform data. The RMS error in arrival time is 28.4 for the unconstrained solution and 18.1 mm when the risetime was fixed.

least squares fit to each waveform, obtaining 2000 noisy estimates of each model parameter, and we examined the error distribution in these estimated parameters. The result of this simulation (Figure 1b) shows a severe correlation between risetime and arrival time having a slope of 1. The RMS scatter of the estimated arrival time about the true arrival time is 28 mm. If we assume that the risetime varies smoothly along the satellite track because it reflects a smoothly varying field of surface waves and we constrain the risetime to the smoothed value, then the RMS scatter in the estimated arrival time is 18 mm, or a 36% reduction in RMS scatter (59% reduction in variance).

[13] Improvements due to retracking of Geosat are characterized in terms of both spatial resolution and noise level. The spatial resolution is estimated by analyzing pairs of sea surface height profiles from nearly collinear tracks and performing a cross-spectral analysis of the height profile pairs, assuming each is a realization of a random process with coherent signal and incoherent noise [*Bendat and Piersol*, 1986], as shown in Figure 2. The power spectra of both signal and noise in sea surface height are shown, before and after retracking. The noise power is cut nearly 50%, resulting in an improvement in spatial resolution of nearly 5 km from 29 km to 24 km. These improvements result in a noticeable sharpening of seafloor tectonic signals, as well as a reduction in false sea surface height variability associated with increased SWH variability (e.g., in the Southern Ocean). The crossover point between signal and noise also indicates that the shortest wavelength resolvable

in an individual Geosat profile is about 24 km in the deep ocean.

[14] To assess the reduction of noise due to retracking, we compare sea surface slope along the GEOSAT GM profiles with the slope from our latest gravity model (version 18), presented in section 2.2. Since the model combines data from both ascending and descending tracks of Geosat, ERS-1,
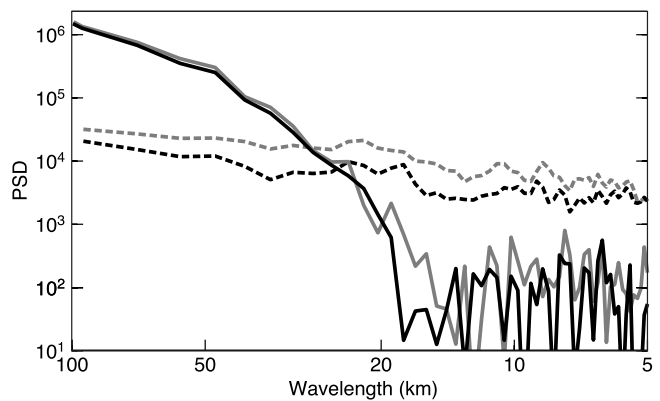

Figure 2. Power spectrum of sea surface height before (gray) and after (black) retracking. Noise spectra are dashed while signal spectra are solid. Retracking cuts noise power by 50% at mesoscale and shorter wavelengths. The spatial resolution is also increased, since the signal power remains above the noise power to shorter wavelengths.

and Topex, the comparison between model slopes and Geosat track slopes is not entirely circular thinking, and it illustrates clearly the improvements due to retracking. Figure 3 shows the RMS difference between along-track slope from Geosat GM and the corresponding slope from north and east vertical deflection grid products averaged at 2 min resolution. The difference profiles are low-pass filtered with a Gaussian filter having a 0.5 gain at wavelengths of 18 km (Figure 3, top and middle) and 80 km (Figure 3, bottom). The RMS of the differences, averaged in $0.25°$ cells, is displayed in Figure 3. The upper RMS difference map uses the original Geosat GM product tracked by the onboard α-β tracker [Lillibridge and Cheney, 1997] sampled at 5 Hz along track. The overall RMS difference is 4.4 μrad. The map shows three categories/areas where the RMS differences exceed the background value ($\sim$2 μrad). First, there are latitudinal bands of high noise especially between $30°$ and $60°$ south latitude. This noise is primarily due to ranging from a surface that is roughened by high waves due to storms and high wind. The second type of high noise area is associated with areas of very high sea surface slope near large seamounts, fracture zones, and spreading ridges. This noise is primarily due to the 1.7 km phase shift of the onboard tracker which causes a misalignment of the sharp feature with the feature recovered in the profile. The third type of noise is due to mesoscale variations in sea surface slope associated with eddies and meandering currents [Cheney et al., 1983].

[15] Figure 3 (middle) shows the same comparison but after retracking the Geosat GM waveforms. The overall RMS difference is reduced to 3.2 μrad which corresponds to a 27% improvement in RMS (47% in variance). Note the noise due to the rough ocean surface is dramatically reduced. Also differences associated with very high sea surface slope are mostly gone. These two reductions in noise are due to the retracking which reduces the sensitivity of the range due to ocean waves and also corrects the phase shift from the onboard tracker. Unfortunately, the "noise" due to mesoscale ocean variability remains. Indeed additional smoothing of the slope differences along track (Figure 3, bottom) further highlights the spatial variations in slope variability and the association of areas of higher variability with deeper [Sandwell and Zhang, 1989] and smoother [Gille et al., 2000] seafloor. Assuming that the RMS differences at wavelengths longer than 80 km are all due to ocean processes, one can estimate the slope error due to ranging noise as 2.8 μrad, which corresponds to 2.8 mGal. Below we will confirm this noise level through a comparison with shipboard gravity measurements.

2.2. Geoid Slope and Gravity Anomaly Model Construction

[16] The marine gravity field model was constructed as described in our previous publication [Sandwell and Smith,

1997] but with the following improvements. The grid cell size was reduced from 2 min to 1 min in an effort to retain higher spatial resolution. The latitude range was extended from $\pm72°$ to $\pm80.7°$ to recover more gravity information in the polar regions. This results in a grid of 2-byte integers with 21,600 columns and 17,280 rows. Our model uses a "remove-restore" procedure to blend short-wavelength detail from satellite altimetry with the large-scale anomalies of geopotential models; in 1997 we used the EGM96 model (complete to degree 360, or 110 km wavelength), while we now use the EGM2008 geoid height model complete to degree and order 2160 including the matching EGM2008 mean dynamic ocean topography (MDOT) model. In the final iteration we also high-pass filter the residual slopes (0.5 gain at 180 km wavelength) to further reduce the influence of unmodeled dynamic ocean topography or tides. The short-wavelength detail is obtained by gridding the residual sea surface slopes along altimeter tracks. In our new model we use more data than in 1997, including retracked data, and we combine the data in a new way, using biharmonic splines with a tension parameter of 0.25 as described by Wessel and Bercovici [1998].

[17] There are two major tasks in our data modeling process. The first task is to build a seamless model of the global marine geoid slope, that is, the north and east components of the deflection of the vertical, by incorporating all available altimeter data and removing the sea surface slope component due to dynamic ocean signals such as tides, mesoscale currents, and their eddies. The second task is to take the geoid slopes obtained in task one and convert them to gravity anomalies. Only in this second task do we employ a gravity field model, such as EGM96 or EGM2008. Our data modeling process produces models of geoid slope as well as gravity anomalies.

[18] To begin the modeling of geoid slope, we remove the UT CSR 4.0 tide model [Bettadpur and Eanes, 1994] from each altimeter profile's sequence of height samples taken at the highest available data rate (10 Hz or 20 Hz, depending on the satellite). The data are low-pass filtered with a cut that begins at 26.8 km wavelength, has 0.5 gain at 14.6 km, and zeros at 10 km; this filter was designed in Matlab using the Parks-McClellan algorithm. After this filter is applied the data can be downsampled to a 5 Hz sampling rate, which corresponds to an along-track spacing of 1.4 km. Because the data in the stacks of GEOSAT ERM and TOPEX were acquired with the onboard tracker, we applied an additional filter to these stacked data to undo (as much as possible) the along-track phase shift and group delay associated with the onboard tracker as described by W. H. F. Smith and D. T. Sandwell (manuscript in preparation, 2009). After this initial filtering we have sea surface height data from all seven data sources in the same form, with the same sampling rate and without phase shifts.

Figure 3. (top) RMS deviation of along-track slopes from the Geosat GM data from onboard tracking with respect to slopes derived from our best estimate of the gravity field (this paper). The global RMS variation is 4.4 μrad. (middle) RMS deviation of along-track slopes from retracked Geosat GM data with respect to slopes derived from our best estimate of the gravity field has a global RMS of 3.19 μrad or a 27% improvement. (bottom) Along-track slope differences (retracked) but low-pass filtered at 80 km wavelength. This RMS deviation of 1.56 μrad is mostly real signal due to mesoscale variations in ocean surface slope.
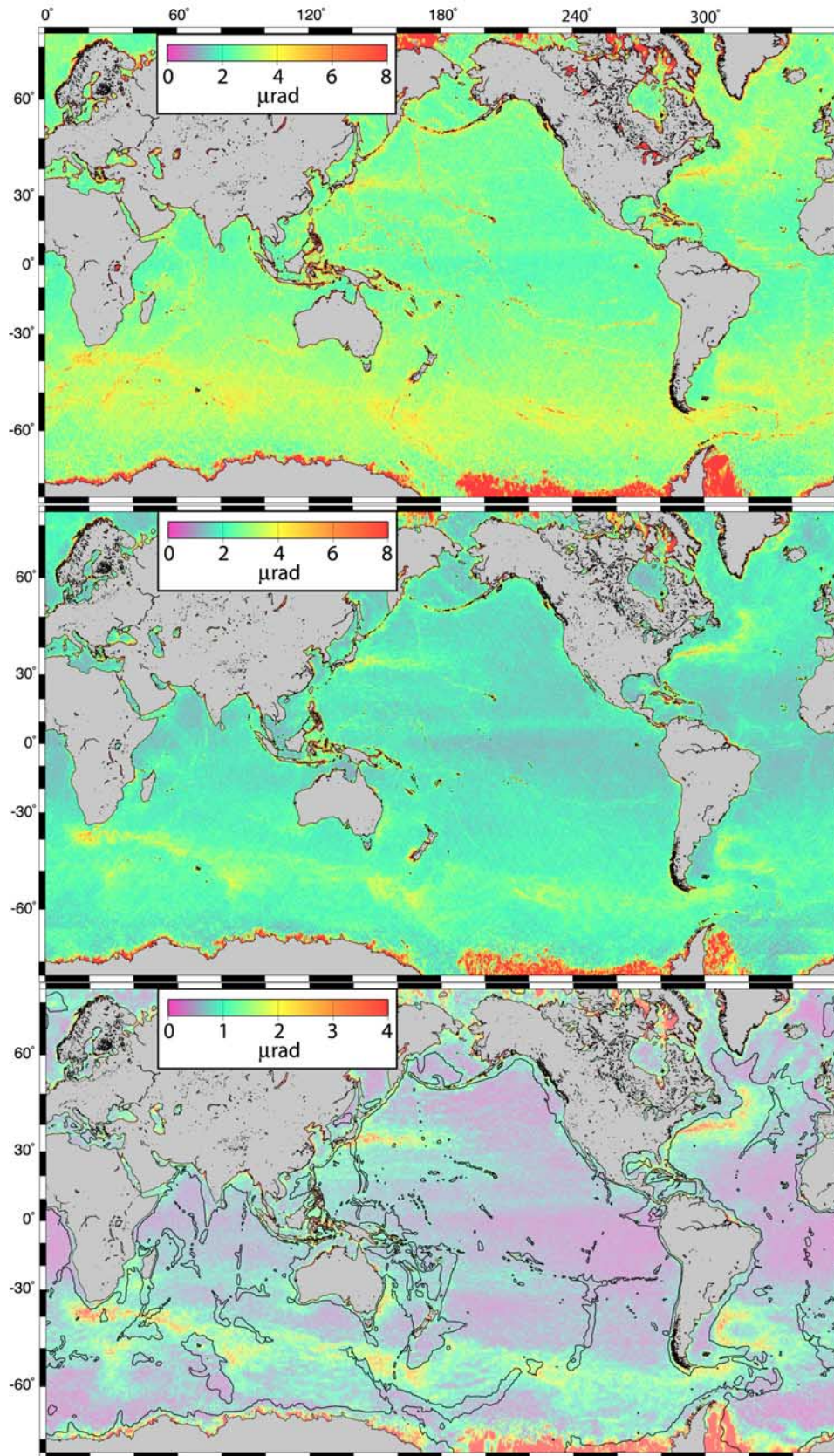
Figure 3

Table 1. Summary of Slope Data and A Priori Uncertainties Used for Gravity Model Construction[a]

	Number of Observations (10^6)	Uncertainty (μrad)
GEOSAT GM	125	8.2
ERS-1 GM	111	9.7
ERS-1 ERM (35-day repeat)	9.2	4.7
GEOSAT ERM (17 day repeat)	4.8	7.5
TOPEX ERM (10 day repeat)	2.8	4.5
TOPEX (maneuver)	20	12.6
ERS GM - polar (threshold retrack)	9.6	30.

[a]Note that these 5 Hz data have minimal along-track filtering (0.5 gain at 9 km wavelength), whereas the low-pass filter applied for the noise analysis shown in Figure 3 was 18 km.

[19] The along-track sea surface slope of each profile is then computed and compared to our prior models of geoid slope, for two reasons. First, the prior model furnishes a sanity check that allows us to detect outliers that produce spurious slopes. Our edit threshold was set at three times the standard deviation given in Table 1. Second, we filter (0.5 gain at 180 km wavelength) the differences in slope between the profile and the model to remove long-wavelength profile slope components due to unmodeled tides, currents, and eddies. After these steps the remaining sea surface slope data are presumed to measure geoid slope, that is, deflection of the vertical. Verification that this is the case comes after the geoid slopes have been converted to gravity anomalies, when we can compare these gravity anomalies to those measured by ships carrying gravimeters.

[20] The conversion of vertical deflections to gravity anomalies is a boundary-value problem for Laplace's equation. The most accurate computations use spherical harmonics at long wavelengths, supplemented by Fourier transforms on data conformally projected onto a flat plane for short wavelengths. We follow a standard practice in geodesy known as a "remove-restore procedure": a spherical harmonic model such as EGM96 or EGM2008 furnishes long-wavelength deflections and gravity anomalies, the deflections are removed from our data, the residual deflections are converted to residual gravity anomalies by Fourier transform, the residual anomalies are then added to the spherical harmonic model anomalies to obtain the total anomaly field.

[21] It is important to understand that use of this procedure does not imply that our model exactly matches the spherical harmonic model at all wavelengths contained in the spherical harmonic model. In principle, if our data disagree with the EGM model at any wavelength, then there will be power in our residual at that wavelength, and so our data may be used to improve the model at all wavelengths. In practice, however, the Fourier transform calculation must be confined to a limited range of latitudes where the conformal projection has a limited range of scales, so that the flat-earth approximation is valid, and this limits the longest wavelengths (~650 km) at which the altimeter data may influence the model. Common practice in geodesy uses "least squares collocation" to model the residual anomalies and usually assumes that the mean value of the residual anomaly will be zero. We find it convenient

to assume that the mean anomaly is small over a patch area for calculating the best spline fit to the seven altimeter data sources, as discussed below.

[22] Our models "feel" the influence of the spherical harmonic model most strongly near shorelines. The altimeter data cannot furnish information about the geoid slope over land, and our residual slopes taper smoothly to zero in land areas. The Laplace boundary value problem is solved as a convolution, so that the gravity anomaly at a point depends on deflections in a region around that point. Our prior models used EGM96, which furnished information to harmonic degree 360, or about 100 km wavelength, and so our solutions began to degrade as one moved closer to shore than 50 km. Our latest solutions use EGM2008, complete to degree 2160, or about 19 km wavelength, so our solutions should feel the lack of land data only about 10 km from shore.

[23] Our model development actually involved two iterations and interactions with the group developing EGM2008 [*Pavlis et al.*, 2008]. First, we constructed a gravity model V16.1 combining all our retracked altimetry and the seven sources of data, but using the EGM96, complete to degree and order 360, as a reference field. The largest source of error in our V16.1 gravity grids is within 50 km of shore [*Maia*, 2006] because of the zeros on land in the residual deflection data. We hoped the group developing EGM2008 might use our deflections at sea; however, they preferred to use the gravity anomalies from our V16.1 field. These ocean data were combined with land and shipboard gravity data as well as longer-wavelength (>400 km) satellite gravity information to construct a new global reference field complete to degree and order 2160 called EGM2007b. The EGM team provided us with this new model, which we then used in our remove/restore procedure to construct a second marine gravity model called V17.1. Because this model included more complete land gravity information during the slope-to-gravity conversion, the errors in nearshore areas were presumably reduced. To reiterate, our north and east deflection grids from version 16.1 and 17.1 are identical; only the gravity models are different and the differences are small except near shorelines. The EGM team then used the V17.1 gravity model in the final construction of EGM2008. Close to the shorelines, the land data available in EGM2008 improves the accuracy of our nearshore marine gravity anomalies.

[24] An additional improvement in our version 18.1 over our version 17.1 comes from the EGM2008 mean dynamic topography model. For version 18.1 we removed the slope of this model from our deflections. The slope of the mean dynamic ocean topography is negligible except where western boundary currents that produce large ocean surface slopes (1–10 μrad) remain spatially fixed over time.

[25] All of these fields (V16–18) use the same along-track altimeter slopes derived from seven data sources as described in Table 1 in their order of importance. Almost all of the gravity information comes from the retracked profiles of the GEOSAT GM and ERS-1 GM. Nevertheless the other data sets provide targeted new information. For example, the 501 tracks of the ERS-1 exact repeat mission (ERM) provide significant new information at high latitudes where the tracks converge and the stacking of multiple cycles provides coverage in ice-free times. The TOPEX ERM data

provide minimal new information along 127 tracks. However, during September of 2002 the TOPEX track was maneuvered to bisect the original 127 tracks. These data, which we call TOPEX maneuver, provide some new information although we show below that the noise level of the data is significantly higher than GEOSAT GM data. Finally we have included some ERS GM data at high latitudes (>65°) that were retracked using a simple threshold retracker. This retracker is able to provide sensible range estimates in ice covered areas where the three-parameter ocean waveform retracker fails. However, these data are extremely noisy and are given very high uncertainty in the least squares estimation process (Table 1).

[26] Prior to filtering, the along-track slope profiles were compared with a previous model to detect and edit outliers; the edit threshold was set at 3 times the standard deviation given in Table 1. Along-track slopes from the EGM2008 geoid plus MDOT model [*Pavlis et al.*, 2008] were removed and the residuals were gridded using a biharmonic spline approach discussed next.

[27] Consider N estimates of slope $s(\mathbf{x_i})$ with direction $\mathbf{n_i}$ each having uncertainty σ_i. We wish to find the "smoothest" surface $w(\mathbf{x})$ that is consistent with this set of data such that $s_i = (\nabla w \bullet \mathbf{n})_i$. As in many previous publications we develop a smooth model using a thin elastic plate that is subjected to vertical point loads [*Briggs*, 1974; *Smith and Wessel*, 1990]. The loads are located at the locations of the data constraints (knots) and their amplitudes are adjusted to match the observed slopes [*Sandwell*, 1987]. To suppress overshooting oscillations of the plate, tension can be applied to its perimeter. *Wessel and Bercovici* [1998] solved this problem by first determining the Greens function for the deflection of a thin elastic plate in tension. The differential equation is

$$\alpha^2 \nabla^4 \phi(\mathbf{x}) - \nabla^2 \phi(\mathbf{x}) = \delta(\mathbf{x}) \qquad (1)$$

where α is a length scale factor that controls the importance of the tension. High α results in biharmonic spline interpolation which minimizes the strain energy in the plate but can produce undesirable oscillations between data points [*Sandwell*, 1987]. Zero α results in harmonic interpolation, which results in a surface that has sharp local perturbations at the locations of the data constraints. The tension factor controls the shape of the interpolating surface. Through experimentation we find good-looking results when the solution is about 0.33 of the way from the biharmonic to the harmonic end-member. The Greens function for this differential operator is

$$\phi(\mathbf{x}) = K_o\left(\frac{|\mathbf{x}|}{\alpha}\right) + \log\left(\frac{|\mathbf{x}|}{\alpha}\right) \qquad (2)$$

where K_o is the modified Bessel function of the second kind and order zero. The smooth surface is a linear combination of these Greens functions each centered at the location of the data constraint.

$$w(\mathbf{x}) = \sum_{j=1}^{N} c_j \phi(\mathbf{x} - \mathbf{x_j}) \qquad (3)$$

The coefficients c_j represent the strength of each point load applied to the thin elastic plate. They are found by solving the following linear system of equations.

$$s_i = (\nabla w \bullet \mathbf{n})_i = \sum_{j=1}^{N} c_j \nabla \phi(\mathbf{x}_i - \mathbf{x}_j) \bullet \mathbf{n_i} \quad i = 1, N \qquad (4)$$

One issue that must be addressed is the possibility of having two data constraints in exactly (or nearly) the same location. This causes the linear system to be exactly singular (or numerically unstable) [*Sandwell*, 1987]. Our satellite altimeter data commonly have many crossing profiles so it is possible to have two or even six slope constraints at nearly the same location. The solution to this problem is to reduce the number of Greens functions (knots) by making sure they are not more closely spaced than some prescribed distance. That minimum distance should be about 1/4 of the shortest wavelength that one hopes to resolve. When the number of knot locations is less than the number of constraints then the linear system is overdetermined and the surface will not exactly match the slope constraints. Since we only wish to match the slopes to within the expected uncertainty of each data type, each equation (4) should be divided by the slope uncertainty to provide the optimal solution using a singular value decomposition algorithm. In our case we are not interested in the absolute height of the surface but just the local slope so our final result is the gradient of the surface.

$$\nabla w(\mathbf{x}) = \sum_{j=1}^{N} c_j \nabla \phi(\mathbf{x} - \mathbf{x_j}) \qquad (5)$$

While this interpolation theory is elegant and very flexible, it is difficult to apply to the altimeter interpolation problem because there are over 200 million observations to grid (Table 1). Consider gridding just 1000 slopes, the matrix of the linear system in equation (4) could have 10^6 elements if all the knot points were retained. In practice we make the following compromises in order to grid this large and diverse set of data.

[28] 1. The data are residuals with respect to the EGM2008 model so we can assemble and grid the data in overlapping small areas. We expect the residuals will only have signal at wavelengths of less than 37 km. Therefore for a 1-min Mercator grid at 70° latitude we use a subarea size of 64 × 64 points, which has a dimension of 40 km (120 km at the equator).

[29] 2. To avoid edge effects, the subareas have 100% overlap and only the inner 32 × 32 interpolated cells are retained. The global analysis has 675 × 539 subareas.

[30] 3. The along-track slope data from each of the six possible slope directions (i.e., ascending and descending profiles from three satellite inclinations ERS, GEOSAT, and TOPEX) and associated uncertainties are binned onto the regularly spaced 1 min Mercator grid, and only the median slope of each type is retained for fitting. At midlatitudes there are typically 2000–3000 slope constraints/uncertainties per subarea and typically 800 unique knot points. The original distribution of knot points matches the satellite tracks so the spacing at the equator can be as small as 1.8 km. We further

Table 2. RMS Altimeter Noise From A Posteriori Comparison With V18 Gravity Model[a]

Tracker		GEOSAT			ERS-1			TOPEX	
		GM Onboard	GM Retrack	ERM Onboard Stack	GM Retrack Ocean	GM Retrack Ice	ERM Stack	Maneuver Onboard	ERM Onboard Stack
$\lambda > 18$ km	a	4.45	**3.21**	**2.18**	**3.57**	**8.62**	**1.75**	**3.34**	**1.17**
	d	4.36	**3.17**	**2.21**	**3.55**	**8.92**	**1.76**	**3.33**	**1.19**
$\lambda > 80$ km	a	1.88	1.56	1.15	1.63	2.98	1.02	1.50	0.73
	d	1.85	1.55	1.15	1.62	3.16	1.02	1.50	0.74

[a]Altimeter noise is measured in μrad. Values in bold represent ascending (a) and descending (d) data used in gravity model construction.

reduce the knot spacing to a minimum of 3 min (5.4 km) which seems to be sufficient to capture all the residual signal for wavelengths >14 km. Since gridding is performed in subareas, the computation time is inversely proportional to the number of CPUs available. This analysis takes about a day of computer time when four processors are used. The results of the computations are grids of residual east and north vertical deflection that are converted to gravity anomalies and vertical gravity gradient as described in our previous publication [*Sandwell and Smith*, 1997]. All grids are finally low-pass filtered using a filter with a 0.5 gain at 16 km, which is close to the cutoff wavelength of the 14.6 km low-pass filter that was applied to the profiles. The combination of the two filters has a cutoff wavelength of about 20 km which provides good looking results that also have low RMS misfit to ground truth gravity anomalies collected by ships. One practical limitation of the current set of altimeter data is that a typical track spacing at the equator is 5 km so one cannot expect to recover wavelengths much shorter than 20 km.

3. Results

3.1. Gravity Accuracy

[31] The resulting vertical deflection and gravity anomaly grids are evaluated using two techniques. First, we examine the rms misfit between the model and the along-track slopes from each of the seven data types. This analysis is good for examining the relative contributions of each of the data types as well as to examine spatial variations in rms misfit. The second analysis compares the model gravity anomalies to gravity anomalies collected by ships. This comparison provides a more independent assessment of data accuracy and resolution but is limited to a few small areas where high-quality shipboard data are available. Indeed, *Maia* [2006] has performed a blind test of an earlier version of this gravity grid (V16.1 EGM96 was used as EGM2008 was not available) and we present a summary of those findings below.

[32] The profile versus model evaluations are provided in Table 2 and Figure 4. Each of the three altimeters has data collected in the exact repeat mission (ERM) configuration as well as the nonrepeat geodetic mission (GM) configuration. For example, 66 repeat cycles of GEOSAT (onboard

tracker) were stacked to form a single GEOSAT ERM profile. The rms deviation is 2.2 μrad for wavelengths greater than 18 km and 1.2 μrad for wavelengths greater than 80 km. The nonstacked GEOSAT GM data have higher RMS difference of 3.2 and 1.6 μrad, respectively. The main features that can be summarized from this analysis are that the retracked GM data have an rms noise level of between 3.2 and 3.6 μrad for wavelengths greater than 18 km. The stacked ERM profiles all have a lower noise level depending approximately on the number of repeat cycles stacked. The noise floor of about 1 μrad is due to a combination of errors such as summarized in Table 3. These estimates of error are maximum values based on independent analyses and, in general, we find the measured noise for wavelengths greater than 80 km to be less than these estimates.

[33] The maps of rms difference shown in Figure 4 (western hemisphere only) reveal the spatial variations in the altimeter noise. The differences from the ERM profiles (maps in left column) are generally less than 1 μrad. Higher rms difference occurs in areas of steep geoid gradient perhaps reflecting the fact that these data were assembled from onboard tracked profiles so the inverse alpha-beta tracker described above does not completely undo the adverse effects of this causal filter. As expected the ERM profiles do not show high RMS differences in the areas of the western boundary currents because both the model and stacked profile represent the long-term average slope across these features. The rms differences of the GM profiles (maps in right column) are generally higher and, as expected, show the time variable effects of the western boundary currents. One step in the slope profile preparation briefly mentioned above is that, prior to regridding, the residual slopes were high-pass filtered using a filter with a 0.5 gain at 180 km wavelength. This filter was designed to remove the time-varying slopes from the GM profiles mainly associated with mesoscale eddies. All the rms difference maps show large differences in areas of seasonal and especially permanent ice cover. These large differences are due to a combination of errors in the model and the profiles. The gravity anomalies in these areas will also be noisy. A more careful retracking of the data in the ice-covered areas can provide significant improvements in gravity anomaly accuracy [*Laxon and McAdoo*, 1994; *McAdoo and Laxon*, 1997].

Figure 4. RMS differences between the along-track slope from altimeter profiles and the new gravity model averaged from 1 min to 2 min resolution. Differences were further filtered with a Gaussian filter having a 0.5 gain at 18 km. The stacked profiles from the exact repeat missions (left column) have lower noise than the geodetic missions.
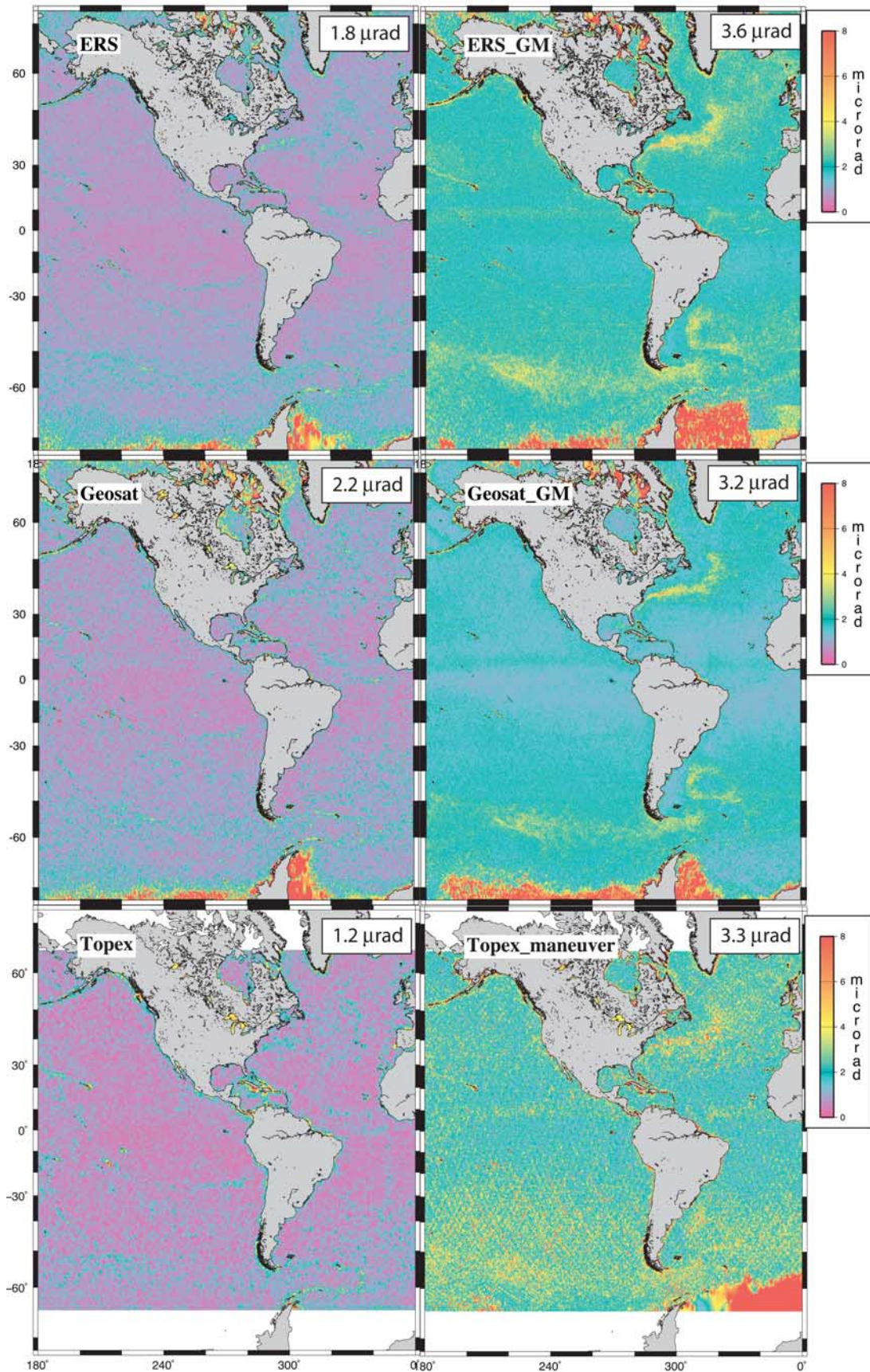
Figure 4

Table 3. Estimated Maximum Error in Sea Surface Slope

Signal or Error Source	Length (km)	Height (cm)	Slope (μrad)
Gravity signal	12–400	1–300	1–300
Orbit errors[a]	8000–20,000	400–1000	<0.5
Ionosphere[b,c]	>900	20	<0.22
Wet troposphere[d]	>100	3–6	<0.6
Sea-state bias[e]	>20	<0.6	<0.3
Inverse barometer[f]	>250	<5	<0.2
Basin-scale circulation (steady)[g]	>1000	100	<1
El Niño, interannual variability, planetary waves[h]	>1000	20	<0.2
Deep ocean tide model errors[d,i]	>1000	3	<0.03
Coastal tide model errors[c,i]	50–100	<13	<2.6
Eddys and mesoscale variability[j]	60–200	30–50	2.5–5
Meandering jet (Gulf Stream)[g]	100–300	30–100	3–10
Steady jet (Florida Current)[g]	100	50–100	5–10

[a]Dynamic orbit determination using the ISS SIGI system, considering errors in force, measurement, attitude, center of mass, and effect of EXPRESS nadir pallet moment arm. This is a worst case error estimate from the "ABYSS" proposal to use the International Space Station. Most satellite altimeters are smaller, simpler in shape, and in higher orbits, all factors which reduce the orbit error [*Shum et al.*, 2009].
[b][*Imel*, 1994].
[c][*Yale*, 1997].
[d][*Chelton et al.*, 2001].
[e][*Monaldo*, 1988].
[f][*Ponte*, 1994].
[g][*Fu and Chelton*, 2001].
[h][*Picaut and Busalacchi*, 2001].
[i][*Shum et al.*, 2001].
[j][*Le-Traon and Morrow*, 2001].

[34]   We compare shipboard profiles with three gravity models to demonstrate the improvements in resolution and accuracy due to retracking and the secondary biharmonic interpolation. The three gravity models are: V9.1 which is based on all the same data used in this paper but both the ERS-1 and GEOSAT GM data are from the original distribution of geophysical data records; V11.1 is like V9.1 but incorporates retracked ERS-1 data [*Sandwell and Smith*, 2005]; and V18.1 (this paper) which has retracked ERS-1, Geosat GM and also uses the biharmonic interpolation as well as the EGM2008 reference model. First it is instructive to show a visual comparison between the three models (Figures 5 and 6). The illuminated gravity anomaly maps for the three cases shows a general decrease in noise level moving from V9.1 to V11.1 and finally to V18.1. The decrease in noise enables one to identify small-scale features such as the small gravity high along the axis of the East Pacific Rise (Figure 5) as well as a field of small uncharted seamounts southwest of the Galapagos Islands (red oval in Figure 5). New features are apparent in V18.1 on the continental margin of South America and the Falkland Plateau (Figure 6). The dramatic improvement in the resolution of the on-land anomalies is due to EGM2008 replacing EGM96.

[35]   A comparison between the three gravity models and shipboard gravity measurements provides a more quantitative assessment of the accuracy of the gravity models. The first example is a west to east trending ship track in the shallow ocean between Indonesia and Borneo (Figure 7). This is a challenging area for gravity field recovery because the altimetry tracks run mainly N–S and the track spacing is greatest at the equator (∼5 km). The gravity anomalies have

relatively short wavelength and low amplitude in relation to the noise. There is a large mean difference between the ship and altimeter-derived gravity that is probably due to an inaccurate gravity tie value in one of the ports [*Wessel and Watts*, 1988]. The RMS difference shows an improvement from 5.6 mGal for V9.1 to 4.8 mGal for V11.1 to 3.03 mGal for V18.1. The overall improvement due to retracking and spline interpolation is 46%. The second example is from a 200 km by 150 km area in the Gulf of Mexico that has been surveyed to submilligal accuracy by EDCON Co (Figure 8). The RMS difference is 3.03 mGal V9.1, 3.26 mGal V11.1 and 2.03 mGal V15.1. This is a 33% improvement in accuracy.

[36]   The third example is from the continental margin area along the east coast of North America (Figure 9). This is a challenging area because the Gulf Stream flows steadily along the east side of the continental margin. This introduces a 5–10 μrad slope in the ocean surface that should not be attributed to a gravity anomaly. In all versions of our gravity field prior to V18, there is a 5–10 mGal error in the gravity along this current. The EGM2008 geoid model also includes a mean dynamic ocean topography (MDOT) model having a resolution of about 200 km wavelength. We added this MDOT to the EGM2008 geoid prior to removing this from the along-track slopes. The false gravity associated with the DOT was not restored in the V18.1 gravity model so the DOT error is minimized. This improvement can be seen through a comparison of a shipboard profile that crosses the continental margin and Gulf Stream several times. The longer wavelength error is reduced from 3.14 mGal to 1.89 mGal. The remaining error is probably associated with inaccurate Eotvos correction for the ship gravity profile which was collected in 1977 prior to GPS navigation [*Wessel and Watts*, 1988]. We have performed numerous comparisons with shipboard profiles and always arrive at about the same rms difference of 2.5 to 3.5 mGal.

[37]   In addition to our in-house comparisons with shipboard gravity we delivered V16.1 of the grid to Marcia Maia at IFREMER to perform some comparisons using shipboard gravity data that were still on proprietary hold [*Maia*, 2006]. Comparisons were performed in two areas, one in the central South Pacific over the Foundation Seamount Chain and a second in the Gulf of Aden. The main findings are that satellite gravity models underestimate the short-wavelength, high-amplitude anomalies (e.g., at submarine volcanoes). A more complete analysis of the gravity field above sharp seamounts confirms this lack of resolution [*Marks and Smith*, 2007]. The quantitative results from the *Maia* [2006] study are provided in Table 4. The raw shipboard gravity contains short wavelength noise at wavelengths shorter than about 10–20 km. When the shipboard data are filtered the RMS differences are between 1.8 and 3.5 mGal with a mean RMS difference of 2.7 mGal.

3.2.   Ridge Segmentation Versus Spreading Rate

[38]   The improved resolution offered by the new global gravity grid and a matching 1-min bathymetry grid discussed in a related publication (Smith and Sandwell, manuscript in preparation, 2009) will be useful for investigating small-scale tectonic processes. For example, these improved resolution grids provide a clearer image of the segmentation of the global spreading ridge. An example of the vertical
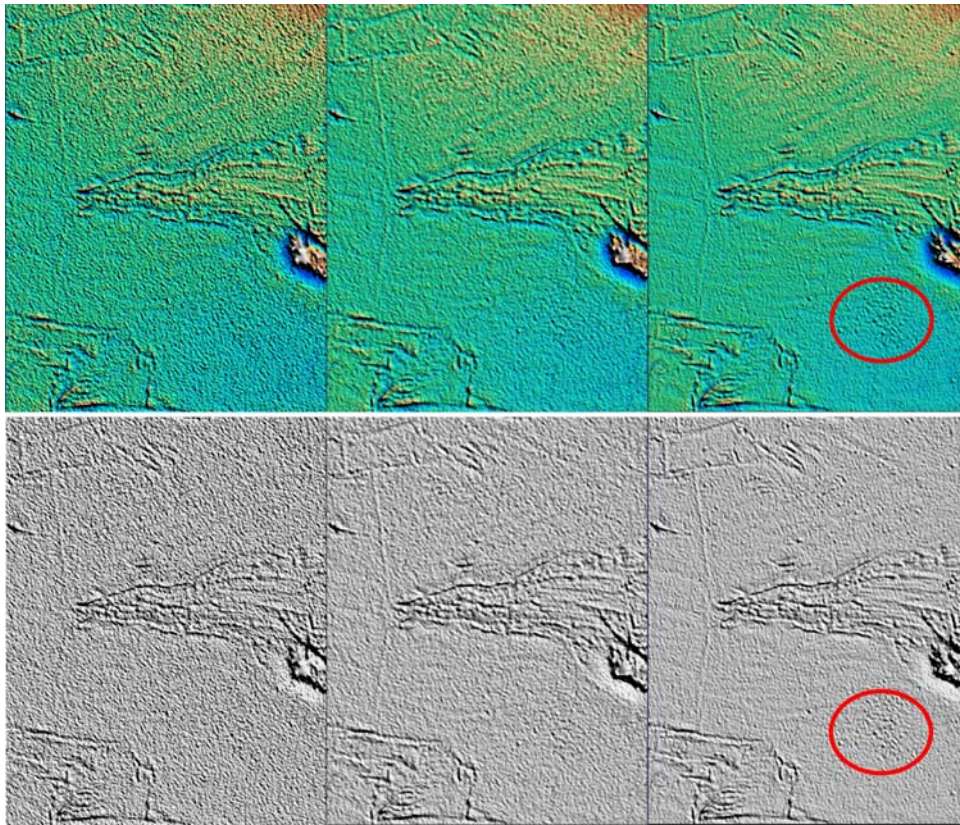
Figure 5. (top) Shaded gravity anomaly for a large region in the Central Pacific Ocean centered at the Galapagos Triple Junction (latitude $11°$ to $-8°$, longitude $255°$ to $270°$). Colors saturate at ±60 mGal. The visual noise level decreases as one moves from V9.1 (left) to V11.1 (center) to V18.1 (right). The axis of the East Pacific Rise is well defined in V18.1 but more difficult to trace in V9.1 because of the higher noise level. The red oval outlines a patch of small uncharted seamounts not apparent in V9.1. (bottom) Vertical gravity gradient, or curvature of the geoid, for the same region.
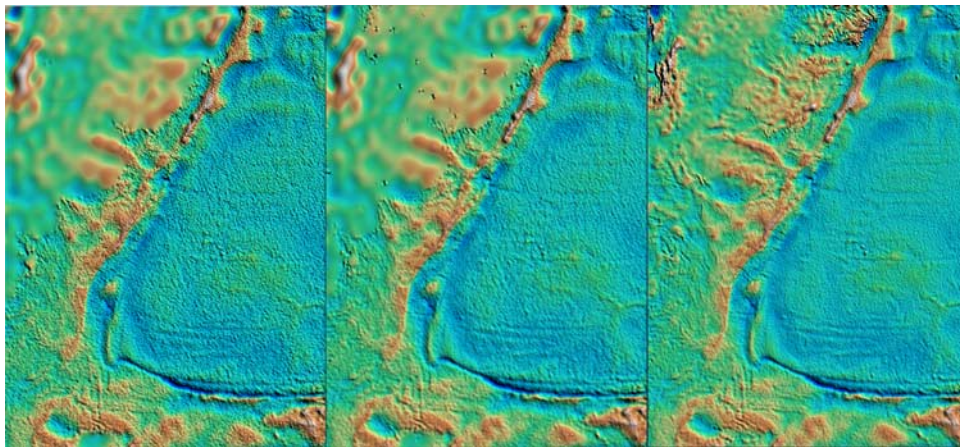
Figure 6. Shaded gravity anomaly for a large region in the South Atlantic centered at the Falkland Basin (latitude $-57°$ to $-27°$, longitude $294°$ to $318°$). Colors saturate at ±80 mGal. The visual noise level decreases as one moves from V9.1 (left) to V11.1 (center) to V18.1 (right). Small-scale gravity structure is visually apparent in V18.1 but hidden in the higher noise of V9.1. Note also the NW-trending striped noise in V11.1 that is largely absent in V18.1. This noise is due to mesoscale ocean variability which has been suppressed by the additional high-pass filter (180 km wavelength) used in V18.1.
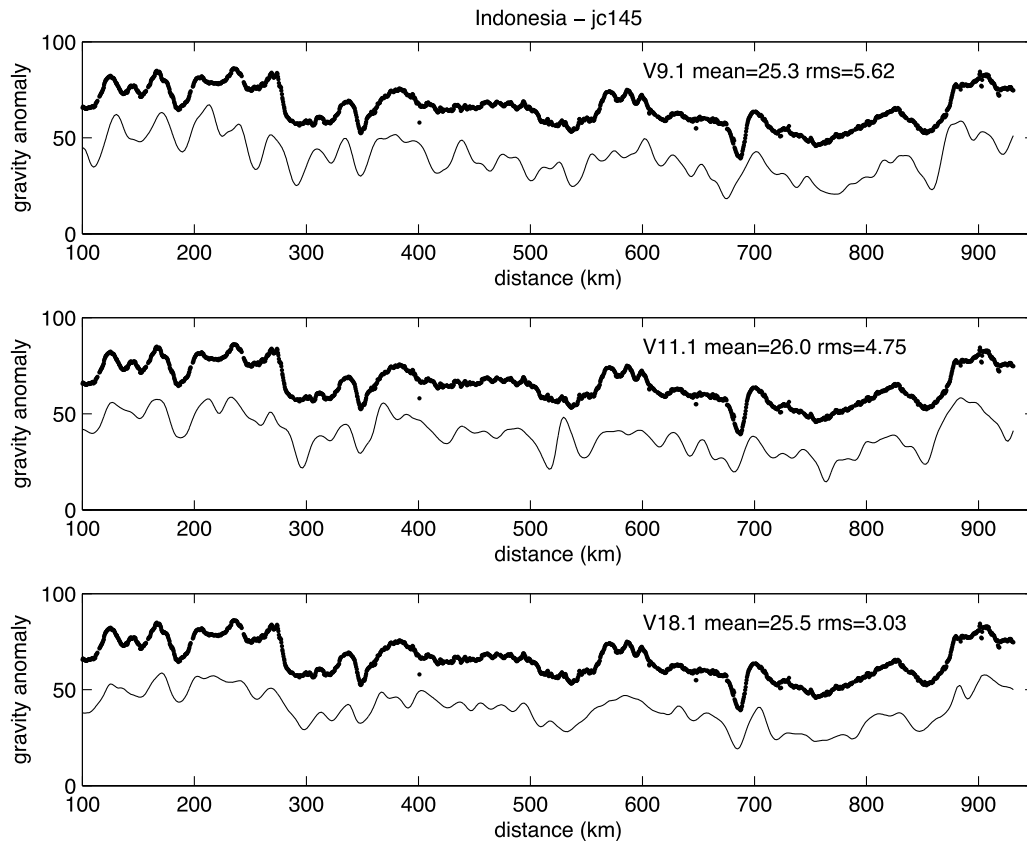
Figure 7. Comparison between satellite-derived gravity models (thin lines) and a shipboard gravity profile (points) across the Java Sea. (top) Gravity model version 9.1 does not use retracked altimeter data and has an RMS misfit of 5.62 mGal. The mean difference of 25 mGal is due to a mean error commonly found in shipboard gravity [*Wessel and Watts*, 1988]. (middle) Gravity model version 11.1 uses retracked ERS-1 altimeter data but the Geosat data were not retracked; the RMS misfit is improved by nearly 1 to 4.75 mGal. (bottom) Gravity model version 18.1 is based on both retracked ERS-1 and Geosat altimeter profiles and also used the biharmonic spline interpolation method. The RMS is improved further to 3.03 mGal, which is a 46% reduction in rms.

gravity gradient used as shading on the new global bathymetry grid at 1 min resolution (Figure 10) helps to delineate the first- and second-order segmentation of the mid-ocean ridges [*Macdonald et al.*, 1988]. A recent study of residual mantle Bouguer anomaly by *Gregg et al.* [2007] using this new V16.1 gravity grid reveals the spreading dependence of gravity anomalies along oceanic transform faults. Their study combined with previous investigations on the variations in ridge-axis morphology with spreading rate [*Menard*, 1967; *Small*, 1994], variations in abyssal hill morphology/seafloor roughness with spreading rate [*Goff*, 1991; *Goff et al.*, 2004; *Small and Sandwell*, 1992; *Smith*, 1998], and the order of magnitude variations in seismic moment release with spreading rate [*Bird et al.*, 2002] highlight the importance of spreading rate in lithospheric strength and crustal structure. This is a first-order aspect of plate tectonics that deserves a more comprehensive analysis.

[39] A more poorly understood phenomenon is the variation in ridge segmentation with spreading rate [*Abbott*, 1986; *Sandwell*, 1986]. A variety of models have been proposed [*Kastens*, 1987] for ridge segmentation including: thermal contraction joints [*Collette*, 1974; *Sandwell*, 1986], thermal bending stresses [*Turcotte*, 1974], segmented mantle upwellings [*Lin and Phipps Morgan*, 1992; *Magde and Sparks*, 1997; *Parmentier and Phipps Morgan*, 1990; *Schouten et al.*, 1985], and minimum energy and damage rheology configurations [*Hieronymus*, 2004; *Lachenbruch*, 1973; *Oldenburg and Brune*, 1975]. Following the discovery of transform faults more than 40 years ago, there is still no consensus on why they exist and why the ridge segmentation varies with spreading rate. A leading hypothesis is that transform faults and fracture zones provide a mechanism for ridge-parallel shrinkage of the lithosphere. However, if this is correct then this mechanism should not be effective on faster spreading ridges where the transform spacing is large. Perhaps other types of cracking and plate bending occur along the fast spreading ridges [*Gans et al.*, 2003; *Sandwell and Fialko*, 2004]. If the plates do not shrink in the ridge-parallel direction then large cracks may penetrate 30 km deep into the lithosphere as proposed by *Korenaga* [2007]. Another possibility is that plates readily contract in all three dimensions. In this case the lateral shrinkage will appear as significant perturbations to the global plate motion models [*Kumar and Gordon*, 2009].

[40] We have begun a more careful analysis of on-ridge and off-ridge segmentation to help resolve these fundamen-
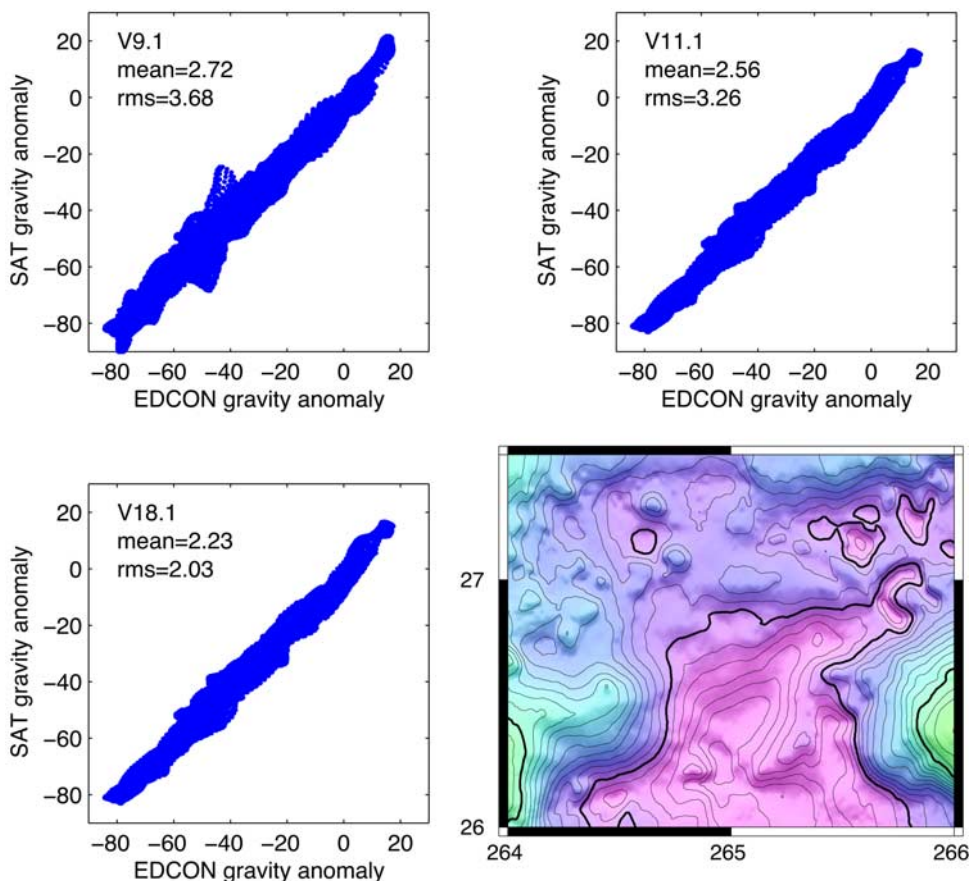
Figure 8. At the bottom right is shown a gravity anomaly map (5 mGal contours) derived from dense shipboard surveys and believed to have submilligal relative accuracy. Also shown are regression plots of satellite gravity versus ship gravity with RMS differences of 3.68 mGal for V9.1, 3.26 mGal for version 11.1, and 2.03 mGal for version 18.1.

tal issues related to cooling of the oceanic lithosphere. Preliminary results are shown in Figures 11 and 12 where we have digitized the first- and second-order discontinuities in the global spreading ridge and display the segment lengths as a function of present-day full spreading rate. The ridges not showing a clear orthogonal pattern of ridges and transforms at this resolution were not analyzed. These include the Reykjanes ridge and the northwest end of the Southwest Indian ridge and the area around the Easter and Juan Fernandez microplates. These preliminary results show a systematic increase in ridge segment length with spreading rate although the relationship is not linear. The gray curve is a Gaussian moving average of the data with a sigma of 20 mm/a. There a change in ridge segment length versus spreading rate that is in accordance with the abrupt change in axial valley topography and gravity anomaly with

spreading rate [*Small and Sandwell*, 1994]. Because the transitions occur at the same intermediate spreading rate, it is likely that a single lithospheric or mantle upwelling mechanism controls both processes. A better understanding of ridge segmentation will require a more complete analysis of both ridge axis and ridge flank data that is now available from our new gravity model.

4. Conclusions

[41] Satellite altimetry has provided the most comprehensive images of the gravity field of the ocean basins with accuracies and resolution approaching typical shipboard gravity data. While many satellite altimeter missions have been flown over the past 3 decades, only 4% of these data have nonrepeat orbital tracks that are necessary for gravity

Figure 9. The map shows gravity anomaly (V18.1, contour interval 10 mGal) of area offshore the east coast of North America where the Gulf Stream follows the continental margin. Track of shipboard gravity profile collected in 1977 is shown by red line. (top and middle) Ship gravity (dots) and satellite gravity (line). The satellite altimeter profiles measure the total slope of the ocean surface, which has a large permanent component that introduces a 5 – 10 mGal error in the V16.1 gravity model. (bottom) Low-pass filtered residual in the satellite gravity are smaller in V18.1 (1.89 mGal) than in V16.1 (3.14 mGal) because of the improved ocean dynamic topography model available in the EGM2008 field used in V18.1.

field recovery. Our analysis uses three approaches to reduce the error in the satellite-derived gravity anomalies to 2–3 mGal from 5 to 7 mGal. First, we have retracked the raw waveforms from 11 months of ERS-1 data [*Sandwell and* *Smith*, 2005] and 18 months of Geosat/GM data (this study) resulting in improvements in range precision of 40% and 27%, respectively. Second, we have used the recently published EGM2008 global gravity model at 5 min resolu-
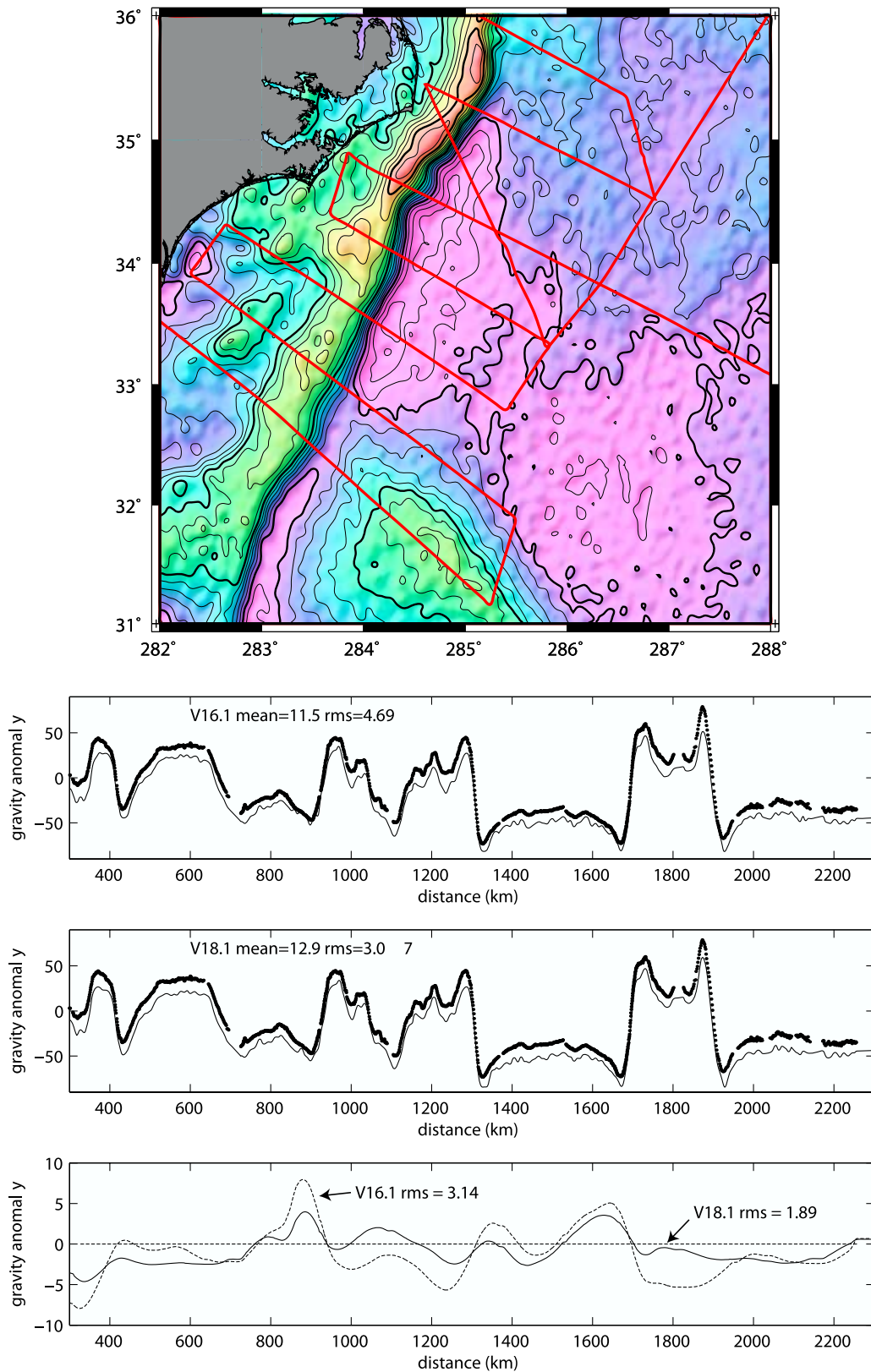

Figure 9

Table 4. RMS Values for the Differences Between the Marine and the Satellite Free Air Anomalies for the V16 Model[a]

Profile	Unfiltered Data	Filtered Data
Profile 1	3.9	3.6 (10 km)
Profile 2	5.4	3.0 (20 km)
Profile 3	4.0	2.6 (20 km)
Profile 4	8.6	1.8 (10 km)
Profile 5	4.0	2.7 (10 km)

[a]RMS is measured in mGal. The second column displays the RMS values for unfiltered marine data. The third column displays the values for filtered data. The cutoff wavelength is shown in brackets. After *Maia* [2006].

tion [*Pavlis et al.*, 2008] in the remove/restore method to provide 5-min resolution gravity over the land and 1-min resolution (8 km 1/2 wavelength) over the ocean with a seamless land to ocean transition. Third we have used a biharmonic spline interpolation method including tension [*Wessel and Bercovici*, 1998] to construct residual vertical deflection grids from seven types of inconsistent along-track slope measurements.

[42] Two approaches are used to evaluate the accuracy and resolution of the new gravity model. Differences between slope measured along satellite altimeter profiles and the along-track slope projected from the vertical deflection grids show two main sources of residual error in the nonrepeat profiles. At smaller length scales (<80 km) the background noise level depends mainly on sea state ranging from 1 to 2 μrad (i.e., 1−2 mGal) in areas of low sea state to 2−3 μrad in areas of higher sea state. At mesoscales (80−300 km wavelength) ocean currents and eddies cause sea

surface slopes to depart from geoid slopes by 3−6 μrad along the western boundary currents and the Antarctic Circumpolar Current. Comparisons between shipboard gravity and the global gravity grid show errors ranging from 2.0 mGal in the Gulf of Mexico to 4.0 mGal in areas with rugged seafloor topography. The largest errors of up to 20 mGal occur on the crests of large seamounts [*Marks and Smith*, 2007]. The main limitation of the gravity model is spatial resolution which is controlled by the spatial filters used in the along-track and 2-D analyses. Because gravity depends on the slope of the ocean surface, and the altimeter measures the sea surface height, which has a nearly white noise spectrum, reducing the size of the filters results in unacceptably high noise levels. We have adopted a compromise filter that has a 0.5 gain at a wavelength of 15 km. A new higher precision altimeter mission having a longer duration could reduce the noise by perhaps 5 times [*Raney et al.*, 2003]. Images of the new gravity model reveal small-scale structure not apparent in the previously published models [e.g., *Sandwell and Smith*, 1997]. In particular the segmentation of the global spreading ridges by orthogonal ridges and transform faults further reveals the variations in ridge axis morphology with spreading rate. As a first step we have digitized the ridge plate boundary and examined the variations in ridge segment length with increasing spreading rate. For rates less than about 60 mm/a the typical ridge segment is 50−80 km long while it increases dramatically at higher rates (100−1000 km). This transition spreading rate of 60 mm/a also marks the transition from axial valley to axial high. We speculate that a single mechanism controls both transitions; candidates include both lithospheric and asthenospheric processes.
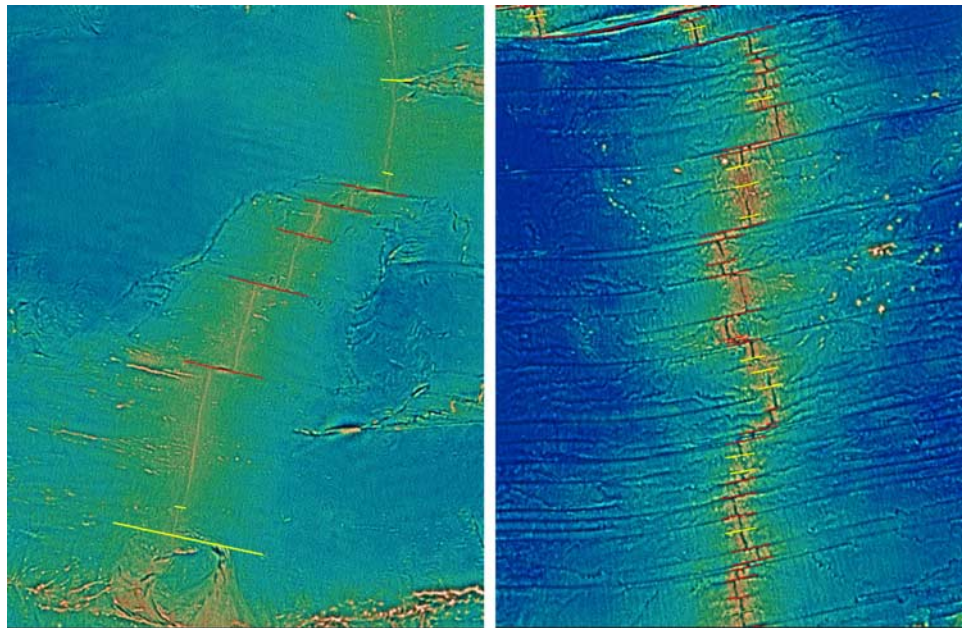

Figure 10. (left) South Pacific bathymetry (color) with vertical gravity gradient superimposed (shading) from the latest bathymetry and gravity grids reveals the first-order (red lines) and second-order (yellow lines) segmentation of the ridges. (right) South Atlantic bathymetry and vertical gravity gradient at same vertical and horizontal scale as the South Atlantic. Ridge segments are much longer along the faster spreading East Pacific Rise than the slower spreading Mid-Atlantic Ridge.
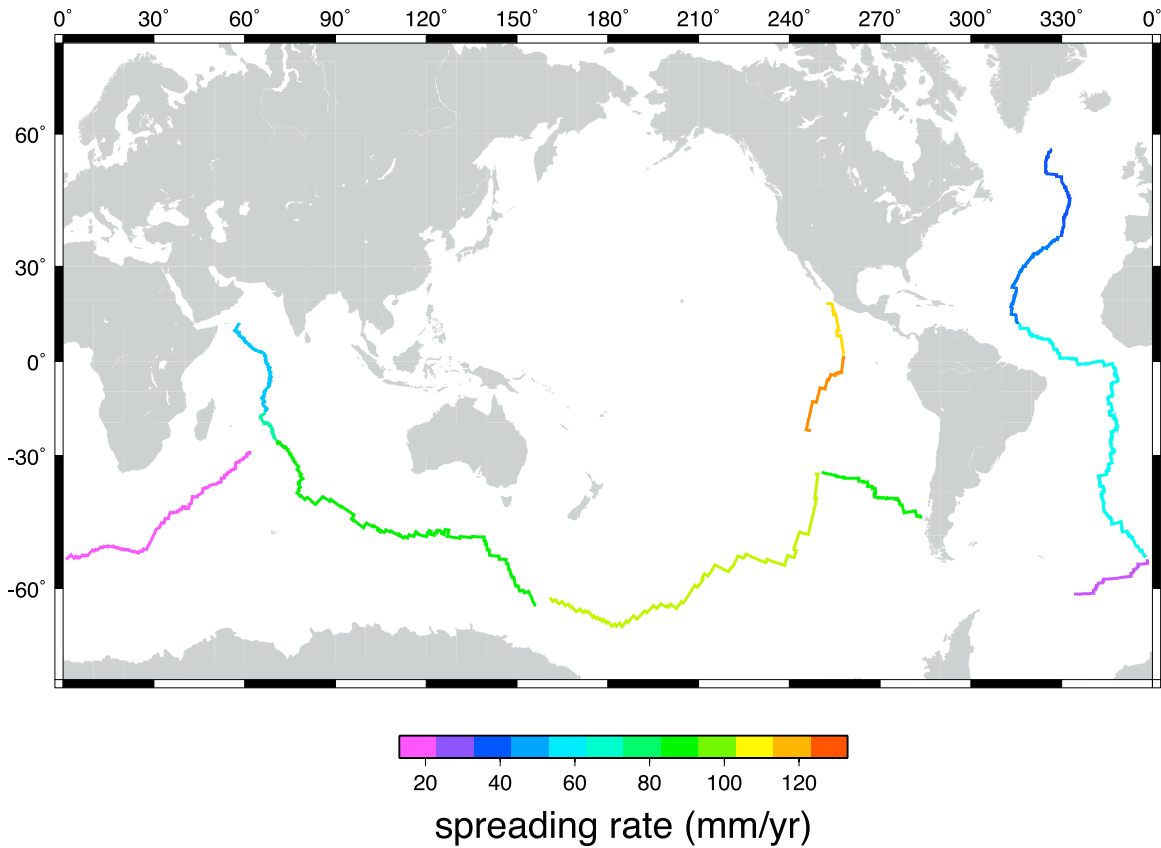
Figure 11.   Present-day spreading rate from *DeMets et al.* [1994] with segments digitized from latest grids.
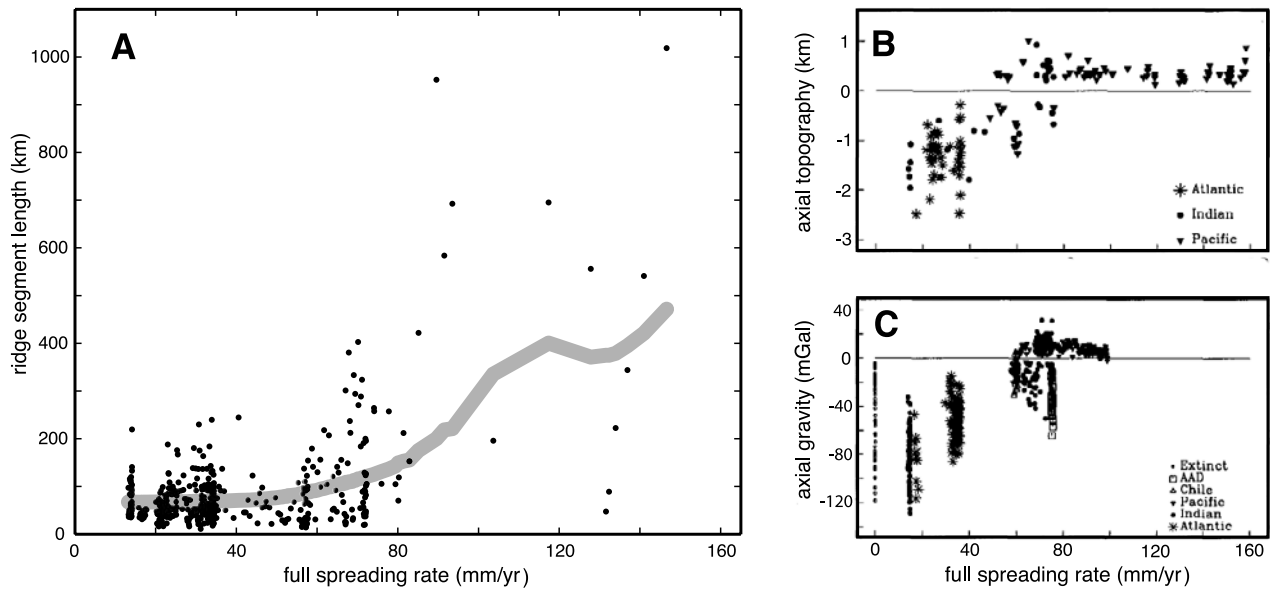

Figure 12.   (a) Preliminary version of ridge segment length versus spreading rate. Grey line is Gaussian moving average (sigma 20 mm/a). For rates less than about 70 mm/a the typical ridge segment length varies from 50 to 100 km. At higher rates there is a wider variation in segment length with some segments 1000 km long. Note that the Reykjanes ridge was not included and there is a lack of transform fault segmentation around the Easter and Juan Fernandez microplates [*Naar and Hey*, 1989]. (b) Axial valley relief and axial gravity amplitude versus full spreading rate from *Small and Sandwell* [1994].

References

Abbott, D. (1986), A statistical correlation between ridge crest offsets and spreading rate, *J. Geophys. Res.*, 13, 157–160.

Amarouche, L., P. Thibaut, O. Z. Zanife, J.-P. Dumont, P. Vincent, and N. Steunou (2004), Improving the Jason-1 ground retracking to better account for attitude effects, *Mar. Geod.*, 27, 171–197, doi:10.1080/01490410490465210.

Andersen, O. B., and P. Knudsen (1998), Global marine gravity field from the ERS-1 and GEOSAT geodetic mission altimetry, *J. Geophys. Res.*, 103, 8129–8137, doi:10.1029/97JC02198.

Baudry, N., and S. Calmant (1991), 3-D Modelling of seamount topography from satellite altimetry, *Geophys. Res. Lett.*, 18, 1143–1146, doi:10.1029/91GL01341.

Bendat, J. S., and A. G. Piersol (1986), *Random Data Analysis and Measurement Procedures*, 2nd ed., 566 pp., John Wiley, New York.

Bettadpur, S. V., and R. J. Eanes (1994), Geographical representation of radial orbit perturbations due to ocean tides: Implications for satellite altimetry, *J. Geophys. Res.*, 99, 24,883–24,898, doi:10.1029/94JC02080.

Bird, P., Y. Y. Kagan, and D. D. Jackson (2002), Plate tectonics and earthquake potential of spreading ridges and oceanic transform faults, in *Plate Boundary Zones*, *Geodyn. Ser.*, vol. 30, edited by S. Stein and J. T. Freymueller, pp. 203–218, AGU, Washington, D.C.

Briggs, I. C. (1974), Machine contouring using minimum curvature, *Geophysics*, 39, 39–48, doi:10.1190/1.1440410.

Brown, G. S. (1977), The average impulse response of a rough surface and its application, *IEEE Trans. Antennas Propag.*, 25(1), 67–74, doi:10.1109/TAP.1977.1141536.

Brown, J., A. Colling, D. Park, J. Phillips, D. Rothery, and J. Wright (1998), *The Ocean Basins: Their Structure and Evolution*, 171 pp., Pergamon, Oxford, U. K.

Cande, S. C., J. M. Stock, R. D. Mueller, and T. Ishihara (2000), Cenozoic motion between East and West Antarctica, *Nature*, 404, 145–150, doi:10.1038/35004501.

Cazenave, A., P. Schaeffer, M. Berge, and C. Brossier (1996), High-resolution mean sea surface computed with altimeter data of ERS-1(Geodetic Mission) and TOPEX-POSEIDON, *Geophys. J. Int.*, 125(3), 696–704, doi:10.1111/j.1365-246X.1996.tb06017.x.

Chelton, D. B., J. C. Reis, B. J. Haines, L. L. Fu, and P. S. Callahan (2001), Satellite altimetry, in *Satellite Altimetry and Earth Sciences*, edited by L. L. Fu and A. Cazenave, pp. 1–131, Academic, San Diego, Calif.

Cheney, R., J. Marsh, and B. Becklet (1983), Global mesoscale variability from collinear tracks of SEASAT altimeter data, *J. Geophys. Res.*, 88, 4343–4354, doi:10.1029/JC088iC07p04343.

Collette, B. (1974), Thermal contraction joints in spreading seafloor as origin of fracture zones, *Nature*, 251, 299–300, doi:10.1038/251299a0.

DeMets, C., R. G. Gordon, D. F. Argus, and S. Stein (1994), Effect of recent revisions to the geomagnetic reversal timescale on estimates of current plate motions, *Geophys. Res. Lett.*, 21, 2191–2194, doi:10.1029/94GL02118.

Dixon, T. H., M. Naraghi, M. K. McNutt, and S. M. Smith (1983), Bathymetric prediction from Seasat altimeter data, *J. Geophys. Res.*, 88, 1563–1571, doi:10.1029/JC088iC03p01563.

Fairhead, J. D., C. M. Green, and M. E. Odegard (2001), Satellite-derived gravity having an impact on marine exploration, *Leading Edge*, 20, 873–876.

Fu, L.-L., and A. Cazenave (2001), *Satellite Altimetry and Earth Sciences: A Handbook of Techniques and Applications*, 463 pp., Academic, San Diego, Calif.

Fu, L.-L., and D. B. Chelton (2001), Large-scale ocean circulation, in *Satellite Altimetry and Earth Sciences*, edited by A. Cazenave and L.-L. Fu, pp. 133–169, Academic, San Diego, Calif.

Gans, K. D., D. S. Wilson, and K. C. Macdonald (2003), Pacific plate gravity lineaments: Extension or thermal contraction?, *Geochem. Geophys. Geosyst.*, 4(9), 1074, doi:10.1029/2002GC000465.

Gille, S. T., M. M. Yale, and D. T. Sandwell (2000), Global correlation of mesoscale ocean variability with seafloor roughness from satellite altimetry, *Geophys. Res. Lett.*, 27(9), 1251–1254, doi:10.1029/1999GL007003.

Goff, J. A. (1991), A global and regional stochastic-analysis of near-ridge abyssal hill morphology, *J. Geophys. Res.*, 96(B13), 21,713–21,737, doi:10.1029/91JB02275.

Goff, J. A., W. H. F. Smith, and K. M. Marks (2004), The contributions of abyssal hill morphology and noise to altimetric gravity fabric, *Oceanography*, 17(1), 24–37.

Gregg, P. C., J. Lin, M. D. Behn, and L. G. J. Montesi (2007), Spreading rate dependence of gravity anomalies along oceanic transform faults, *Nature*, 448, 183–187, doi:10.1038/nature05962.

Haxby, W. F., and J. K. Weissel (1986), Evidence for small-scale mantle convection from Seasat altimeter data, *J. Geophys. Res.*, 91(B3), 3507–3520, doi:10.1029/JB091iB03p03507.

Haxby, W. F., G. D. Karner, J. L. LaBrecque, and J. K. Weissel (1983), Digital images of combined oceanic and continental data sets and their use in tectonic studies, *Eos Trans. AGU*, 64(52), 995–1004.

Hieronymus, C. F. (2004), Control on seafloor spreading geometries by stress- and strain-induced lithospheric weakening, *Earth Planet. Sci. Lett.*, 222, 177–189, doi:10.1016/j.epsl.2004.02.022.

Hwang, C., and B. Parsons (1996), An optimal procedure for deriving marine gravity from multi-satellite altimetry, *J. Geophys. Int.*, 125, 705–719, doi:10.1111/j.1365-246X.1996.tb06018.x.

Imel, D. A. (1994), Evaluation of the TOPEX/POSEIDON dual-frequency ionospheric correction, *J. Geophys. Res.*, 99, 24,895–24,906, doi:10.1029/94JC01869.

Jayne, S. R., L. C. St. Laurent, and S. T. Gille (2004), Connections between ocean bottom topography and the Earth's Climate, *Oceanography*, 17(1), 65–74.

Jung, W. Y., and P. R. Vogt (1992), Predicting bathymetry from Geosat-ERM and shipborne profiles in the South Atlantic ocean, *Tectonophysics*, 210, 235–253, doi:10.1016/0040-1951(92)90324-Y.

Kastens, K. K. (1987), A compendium of causes and effects of processes at transform faults and fracture zones, *Rev. Geophys.*, 25(7), 1554–1562, doi:10.1029/RG025i007p01554.

Klees, R., R. Koop, P. Visser, and J. van den IJssel (2000), Efficient gravity field recovery from GOCE gravity gradient observations, *J. Geod.*, 74(7–8), 561–571, doi:10.1007/s001900000118.

Korenaga, J. (2007), Thermal cracking and deep hydration of oceanic lithosphere: A key to generation of plate tectonics?, *J. Geophys. Res.*, 112, B05408, doi:10.1029/2006JB004502.

Kumar, R. R., and R. G. Gordon (2009), Horizontal thermal contraction of oceanic lithosphere: The ultimate limit to the rigid plate approximation, *J. Geophys. Res.*, 114, B01403, doi:10.1029/2007JB005473.

Kunze, E., and S. G. Llewellyn Smith (2004), The role of small-scale topography in turbulent mixing of the global ocean, *Oceanography*, 17(1), 55–64.

Lachenbruch, A. H. (1973), A simple mechanical model for oceanic spreading centers, *J. Geophys. Res.*, 78, 3395–3417, doi:10.1029/JB078i017p03395.

Lawver, L. A., L. M. Gahagan, and M. F. Coffin (1992), The development of paleoseaways around Antarctica, in *The Antarctic Paleoenvironment: A Perspective on Global Change, Geophys. Monogr. Ser.*, vol. 56, edited by J. P. Kennett and D. A. Warnke, pp. 7–30, AGU, Washington, D. C.

Laxon, S., and D. McAdoo (1994), Arctic Ocean gravity field derived from ERS-1 satellite altimetry, *Science*, 265(5172), 621–624, doi:10.1126/science.265.5172.621.

Lemoine, F. G., et al. (1998), The development of the joint NASA CSFC and the national Imagery and Mapping Agency (NIMA) geopotential model EGM96, 320 pp., NASA Goddard Space Flight Cent., Greenbelt, Md.

Le-Traon, P.-Y., and R. Morrow (2001), Ocean currents and eddies, in *Satellite Altimetry and Earth Sciences*, edited by A. Cazenave and L.-L. Fu, pp. 175–215, Academic, San Diego, Calif.

Lillibridge, J., and R. Cheney (1997), The Geosat Altimeter JGM-3 GDRs [CD-ROM], NOAA, Silver Spring, Md.

Lillibridge, J. L., W. H. F. Smith, R. Scharrroo, and D. T. Sandwell (2004), The Geosat geodetic mission 20th anniversary data product, *Eos Trans. AGU*, 85(47), Fall Meet. Suppl., Abstract SF43A–0786.

Lin, J., and J. Phipps Morgan (1992), The spreading rate dependence of three-dimensional mid-ocean ridge gravity structure, *Geophys. Res. Lett.*, 19, 13–16, doi:10.1029/91GL03041.

Macdonald, K. C., P. J. Fox, L. J. Perram, M. F. Eisen, R. M. Haymon, S. P. Miller, S. M. Carbotte, M. H. Cormier, and A. N. Shor (1988), A new view of the mid-ocean ridge from the behavior of ridge-axis discontinuities, *Nature*, 335(6187), 217–225, doi:10.1038/335217a0.

Magde, L. S., and D. W. Sparks (1997), Three-dimensional mantle upwelling, melt generation, and melt migration beneath segment slow spreading ridge, *J. Geophys. Res.*, 102, 20,571–20,583, doi:10.1029/97JB01278.

Maia, M. (2006), Comparing the use of marine and satellite data for geodynamic studies, paper presented at 15 Years of Progress in Radar Altimetry Symposium, Eur. Space Agency, Venice, Italy.

Marks, K. M., and W. H. F. Smith (2007), Some remarks on resolving seamounts in satellite gravity, *Geophys. Res. Lett.*, 34, L03307, doi:10.1029/2006GL028857.

Maus, S., C. M. Green, and J. D. Fairhead (1998), Improved ocean-geoid resolution from retracked ERS-1 satellite altimeter waveforms, *Geophys. J. Int.*, *134*(1), 243–253, doi:10.1046/j.1365-246x.1998.00552.x.

McAdoo, D., and S. Laxon (1997), Antarctic tectonics: Constraints from an ERS-1 satellite marine gravity field, *Science*, *276*(5312), 556–561, doi:10.1126/science.276.5312.556.

Menard, H. W. (1967), Sea floor spreading topography and second layer, *Science*, *157*(3791), 923–924, doi:10.1126/science.157.3791.923.

Menke, W. (1991), Applications of the POCS inversion method to interpolating topography and other geophysical fields, *Geophys. Res. Lett.*, *18*(3), 435–438, doi:10.1029/90GL00343.

Monaldo, F. (1988), Expected differences between buoy and radar altimeter estimates of wind speed and significant wave height and their implications on buoy-altimeter comparisons, *J. Geophys. Res.*, *93*(C3), 2285–2302, doi:10.1029/JC093iC03p02285.

Mueller, R. D., W. R. Roest, J.-Y. Royer, L. M. Gahagan, and J. G. Sclater (1997), Digital isochrons of the world's ocean floor, *J. Geophys. Res.*, *102*, 3211–3214, doi:10.1029/96JB01781.

Munk, W., and C. Wunch (1998), Abyssal recipes II: Energetics of today and wind mixing, *Deep Sea Res., Part I*, *45*, 1977–2010, doi:10.1016/S0967-0637(98)00070-3.

Naar, D. F., and R. N. Hey (1989), Speed limit for oceanic transform faults, *Geology*, *17*(5), 420–422, doi:10.1130/0091-7613(1989)017<0420:SLFOTF>2.3.CO;2.

Oldenburg, D. W., and J. N. Brune (1975), An explanation for the orthogonality of ocean ridges and transform faults, *J. Geophys. Res.*, *80*(17), 2575–2585, doi:10.1029/JB080i017p02575.

Parmentier, E. M., and J. Phipps Morgan (1990), Spreading rate dependence of three-dimensional structure in oceanic spreading centres, *Nature*, *348*, 325–328, doi:10.1038/348325a0.

Pavlis, N. K., S. A. Holmes, S. C. Kenyon, and J. K. Factor (2007), Earth gravitational model to degree 2160: Status and progress, paper presented at XXIV General Assembly, pp. 2–13, Int. Union of Geod. and Geophys., Perugia, Italy.

Pavlis, N. K., S. A. Holmes, S. C. Kenyon, and J. K. Factor (2008), An Earth gravitational model to degree 2160, paper presented at General Assembly, Eur. Geosci. Union, Vienna.

Picaut, J., and A. J. Busalacchi (2001), Tropical ocean variability, in *Satellite Altimetry and Earth Sciences*, edited by A. Cazenave and L.-L. Fu, pp. 217–236, Academic, San Diego, Calif.

Ponte, R. M. (1994), Understanding the relation between wind- and pressure-driven sea level variability, *J. Geophys. Res.*, *99*, 8033–8039, doi:10.1029/94JC00217.

Ramillien, G., and A. Cazenave (1997), Global bathymetry derived from altimeter data of the ERS-1 Geodetic Mission, *J. Geodyn.*, *23*(2), 129–149, doi:10.1016/S0264-3707(96)00026-9.

Raney, R. K., W. H. F. Smith, D. T. Sandwell, J. R. Jensen, D. L. Porter, and E. Reynolds (2003), Abyss-Lite: Improved bathymetry from a dedicated small satellite delay-Doppler radar altimeter, paper presented at International Geoscience and Remote Sensing Symposium IGARSS2003, IEEE, Toulouse, France.

Reigber, C., et al. (2002), A high quality global gravity field model from CHAMP GPS tracking data and accelerometer (EIGEN-1S), *Geophys. Res. Lett.*, *29*(14), 1692, doi:10.1029/2002GL015064.

Rummel, R., and R. H. N. Haagmans (1990), Gravity gradients from satellite altimetry, *Mar. Geod.*, *14*, 1–12.

Sandwell, D. T. (1984), A detailed view of the South Pacific from satellite altimetry, *J. Geophys. Res.*, *89*, 1089–1104, doi:10.1029/JB089iB02p01089.

Sandwell, D. T. (1986), Thermal stress and the spacings of transform faults, *J. Geophys. Res.*, *91*, 6405–6417, doi:10.1029/JB091iB06p06405.

Sandwell, D. T. (1987), Biharmonic spline interpolation of Geos-3 and Seasat altimeter data, *Geophys. Res. Lett.*, *14*(2), 139–142, doi:10.1029/GL014i002p00139.

Sandwell, D., and Y. Fialko (2004), Warping and cracking of the Pacific plate by thermal contraction, *J. Geophys. Res.*, *109*, B10411, doi:10.1029/2004JB003091.

Sandwell, D. T., and W. H. F. Smith (1997), Marine gravity anomaly from Geosat and ERS-1 satellite altimetry, *J. Geophys. Res.*, *102*, 10,039–10,054, doi:10.1029/96JB03223.

Sandwell, D. T., and W. H. F. Smith (2005), Retracking ERS-1 altimeter waveforms for optimal gravity field recovery, *Geophys. J. Int.*, *163*, 79–89, doi:10.1111/j.1365-246X.2005.02724.x.

Sandwell, D. T., and B. Zhang (1989), Global mesoscale variability from the Geosat exact repeat mission: Correlation with ocean depth, *J. Geophys. Res.*, *94*, 17,971–17,984, doi:10.1029/JC094iC12p17971.

Schouten, H., K. D. Klitgord, and J. A. Whitehead (1985), Segmentation of mid-ocean ridges, *Nature*, *317*, 225–229, doi:10.1038/317225a0.

Shum, C. K., et al. (2001), Recent advances in ocean tidal science, *J. Geod. Soc. Jpn.*, *47*(1), 528–537.

Shum, C. K., P. A. M. Abusali, H. Lee, J. Ogle, R. K. Raney, J. C. Reis, W. H. F. Smith, D. Svehla, and C. Zhao (2009), Science requirements for ABYSS: A proposed Space Station RADAR altimeter to map global bathymetry, *IEEE Trans. Geosci. Remote Sens.*, in press.

Small, C. (1994), A global analysis of mid-ocean ridge axial topography, *Geophys. J. Int.*, *116*, 64–84, doi:10.1111/j.1365-246X.1994.tb02128.x.

Small, C., and D. T. Sandwell (1992), An analysis of ridge axis gravity roughness and spreading rate, *J. Geophys. Res.*, *97*(B3), 3235–3245, doi:10.1029/91JB02465.

Small, C., and D. T. Sandwell (1994), Imaging mid-ocean ridge transitions with satellite gravity, *Geology*, *22*, 123–126.

Smith, W. H. F. (1998), Seafloor tectonic fabric from satellite altimetry, *Annu. Rev. Earth Planet. Sci.*, *26*(1), 697–747, doi:10.1146/annurev.earth.26.1.697.

Smith, W. H. F., and D. T. Sandwell (1994), Bathymetric prediction fron dense satellite altimetry and sparse shipboard bathymetry, *J. Geophys. Res.*, *99*, 21,803–21,824, doi:10.1029/94JB00988.

Smith, W. H. F., and D. T. Sandwell (1997), Global sea floor topography from satellite altimetry and ship depth soundings, *Science*, *277*(5334), 1956–1962, doi:10.1126/science.277.5334.1956.

Smith, W. H. F., and P. Wessel (1990), Gridding with continuous curvature splines in tension, *Geophysics*, *55*(3), 293–305, doi:10.1190/1.1442837.

Tapley, B. D., and M. C. Kim (2001), Applications to geodesy, in *Satellite Altimetry and Earth Sciences*, edited by A. Cazenave and L.-L. Fu, pp. 371–403, Academic, San Diego, Calif.

Tapley, B., et al. (2005), GGM02 - An improved Earth gravity model from GRACE, *J. Geod.*, *79*, 467–478, doi:10.1007/s00190-005-0480-z.

Turcotte, D. L. (1974), Are transform faults thermal contraction cracks?, *J. Geophys. Res.*, *79*, 2573–2577, doi:10.1029/JB079i017p02573.

Wessel, P., and D. Bercovici (1998), Interpolation with splines in tension: A Green's function approach, *Math. Geol.*, *30*(1), 77–93, doi:10.1023/A:1021713421882.

Wessel, P., and A. B. Watts (1988), On the accuracy of marine gravity measurements, *J. Geophys. Res.*, *93*(B1), 393–413, doi:10.1029/JB093iB01p00393.

Yale, M. M. (1997), Modeling upper mantle rheology with numerical experiments and mapping marine gravity with satellite altimetry, Ph.D. thesis, 118 pp., Univ. of Calif., San Diego, La Jolla.

_____

D. T. Sandwell, Scripps Institution of Oceanography, University of California, San Diego, La Jolla, CA 92093-0225, USA. (dsandwell@ucsd.edu)

W. H. F. Smith, Laboratory for Satellite Altimetry, NOAA, 1335 East-West Highway, Room 5408, Silver Spring, MD 20910, USA.